J. Chem. Theory Comput. **2010,** *6,* 2809–2821

2809

Calculation of One- and Two-Photon Absorption Spectra of Thiolated Gold Nanoclusters using Time-Dependent Density Functional Theory

Paul N. Day,*,[†,‡] Kiet A. Nguyen,[†,§] and Ruth Pachter*,[†]

Materials and Manufacturing Directorate, Air Force Research Laboratory, Wright Patterson Air Force Base, Ohio 45433, General Dynamics Information Technology, Inc., 5200 Springfield Street, Dayton, Ohio 45431, and UES, Inc., 4401 Dayton Xenia Road, Dayton, Ohio 45432

Abstract: The one- (OPA) and two-photon (TPA) absorption spectra have been calculated for a gold dimer, for a monothiolated gold dimer anion, for a thiolated gold cluster $[Au_{25}(SH)_{18}]^{-1}$, whose structure has been determined, and for a proposed cluster $[Au_{12}(SR)_9]^{+1}$ using time-dependent density functional theory (TDDFT). Geometry optimization with different exchange−correlation (X-C) functionals yielded small differences which had significant consequences in the spectra calculations. The calculated excitation energies of $Au_{25}(SH)_{18}^{-1}$ are in excellent agreement with experiment when the local density approximation Xα-optimized geometry is used with the B3LYP X-C functional. The CAMB3LYP and mCAM functionals yielded OPA results in good agreement with experiment for the dimer systems and the larger clusters. The super-atom theory was useful in analyzing the electronic transitions in the larger clusters. TPA was dominated by resonance effects, and the calculated cross-sections displayed a strong X-C functional dependence.

I. Introduction

Gold clusters that are smaller than about 1 nm show quantum effects,[1−3] and clusters with 25 gold atoms have recently been reported to exhibit large two-photon absorption (TPA)[2,4] and to be capable of serving as a platform for ligand exchange with chiral ligands.[5] The structure of the $[Au_{25}(SR)_{18}]^{-1}$ complex was successfully predicted theoretically by Akola et al.[6] for R = CH_3 and determined experimentally by Heaven et al.[7] and by Zhu et al.[3] for R = CH_2CH_2Ph. The structure, shown in Figure 1 with R = H, has an Au_{13} icosohedral core with one Au atom at each vertex of the icosohedron and one at the center. This icosohedral core is surrounded by three pairs of V-shaped structures, (−SR−Au−SR−Au−SR−). These three pairs of Vs are in orthogonal planes which are mirror planes in the icosohedral core, reducing the effective symmetry of the
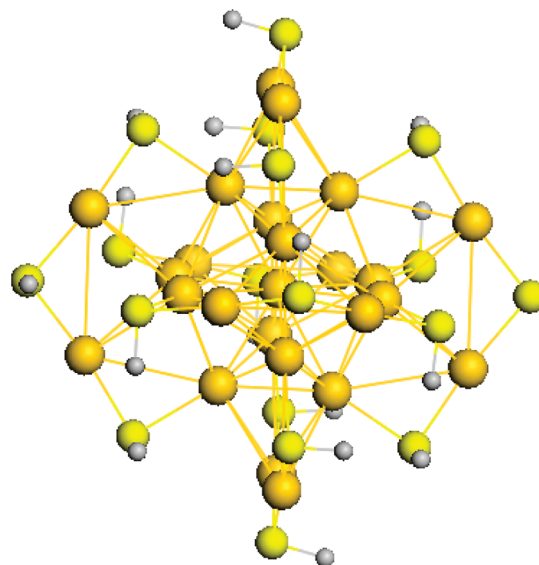
Figure 1. Optimized structure of $Au_{25}(SH)_{18}^{-1}$.

molecule to D_{2h}. Each vertex atom in the icosohedral core is bonded to a sulfur atom. Of the 20 triangular faces in the

---

* Corresponding authors. E-mail: Paul.Day@wpafb.af.mil (P.N.D.) or Ruth.Pachter@wpafb.af.mil (R.P.).

[†] Wright Patterson Air Force Base.

[‡] General Dynamics Information Technology, Inc.

[§] UES, Inc.

icosohedral core, 12 are covered by an outer gold atom, while the other 8 faces appear unprotected.

A theory for magic number stabilities of gold clusters has been proposed by Walter et al.[8] based in part on an earlier super-atom theory which produced magic numbers for sodium atom clusters, as shown by Knight et al.[9] and theorized by Ekardt.[10,11] The magic numbers occur when the number of valence electrons in the super-atom corresponds to a strong electron shell closure. Analogous with the atomic s and p orbitals, filling the 1S super-atom shell gives a magic number of 2 and filling the 1S and 1P shells gives a magic number of 8. The number of valence electrons n^* is given by

$$n^* = N\nu_A - M - z$$

where N is the number of gold atoms, ν_A is the valence of the gold atom (assumed to be 1), M is the number of electron-withdrawing ligands, and z is the net charge of the molecule. Thus, for $[Au_{25}(SR)_{18}]^{-1}$, n^* is equal to 8, corresponding to the super-atom electron occupation $1S^2 1P^6$, while for $Au_{102}(SR)_{44}$, for which the structure has been determined by Jadzinsky et al.,[1] n^* is equal to 58, corresponding to the occupation $1S^2 1P^6 1D^{10} 2S^2 1F^{14} 2P^6 1G^{18}$. This formula was exploited by Jiang and Dai[12] to design molecules based on $[Au_{25}(SR)_{18}]^{-1}$ but with a different central atom; they adjusted the charge z in order to maintain $n^* = 8$. Since 2 is also a magic number, both the gold dimer and its simplest thiolated anionic structure, $[Au_2(SR)]^{-1}$, should be stable. The gold dimer has been studied previously both experimentally[13-19] and theoretically,[20-23] but to our knowledge $[Au_2(SR)]^{-1}$ has not been previously studied. We have therefore investigated these systems as well as a previously proposed[24] structure for the smallest thiolated gold super-atom complex, $Au_{12}(SR)_9^{+1}$, to test the effect of the sulfur ligands on the absorption spectrum of very small gold clusters.

Overall, theoretical studies[25,26] have indicated only a weak dependence of structure, energetics, and spectra on the size of the alkyl group in gold alkyl thiolates as well as on the solvent environment. The proposed reason for the small effects of solvent and ligand size on the absorption spectrum of $[Au_{25}(SR)_{18}]^{-1}$ is that the relevant transitions are primarily in the gold core. The linear absorption spectrum for $[Au_{25}(SR)_{18}]^{-1}$ has been measured in water with SR = glutathione,[27] in toluene[28] and hexane[2,4] with R = n-hexyl, and in toluene with R = ethyl phenyl,[3] and they are all in good agreement, again indicating a weak dependence on the ligand size and the solvent. Thus, in this study, for computational economy, we will focus on the smallest possible ligand with R = H for the thiolated Au_{25} cluster, and we have not included any solvent effects in the calculations.

Although time-dependent density functional theory (TDDFT) has been used to calculate the spectra for gold clusters as large as 146 gold atoms[29] as well as for $[Au_{25}(SR)_{18}]^{-1}$ using several functionals,[26] this work is the first to include hybrid functionals to determine the dependence of the calculated spectra on the choice of X-C functional. In this work, we study the absorption spectrum for $[Au_{25}(SH)_{18}]^{-1}$, in comparison to experiment[2-4,27,28] and previous calculations.[3,26] Moreover, we extend the calcula-

tions to explain the large TPA cross-sections that have been reported from experiment.[2,4]

II. Theory

The expression for calculating the TPA cross-section has been given previously[30-34]

$$\delta_{f0}(E_1 + E_2) = \frac{8\pi^4}{(ch)^2} E_1 E_2 g(E_1 + E_2)|S_{f0}(u_1, u_2)|^2 \quad (1)$$

where g is a line width function, $|S_{f0}(u_1,u_2)|^2$ is the two-photon probability corresponding to a transition from the ground (0) to a final state (f),[35-43]

$$|S_{f0}(u_1, u_2)|^2 = \left| \sum_i^N \left[\frac{(\mathbf{u}_1 \cdot \mu_{i0})(\mu_{fi} \cdot \mathbf{u}_2)}{E_i - E_1 + i\Gamma_i} + \frac{(\mathbf{u}_2 \cdot \mu_{i0})(\mu_{fi} \cdot \mathbf{u}_1)}{E_i - E_2 + i\Gamma_i} \right] \right|^2$$

$$(2)$$

and E_1 and E_2 are the energies of the two photons with unit polarization vectors $\mathbf{u}_1$ and $\mathbf{u}_2$, respectively. The transition dipole moments are given by μ_{ij}, the state energies by E_i, and the state decay constants by Γ_i. In molecules which are close to being centrosymmetric, the TPA cross-section can be estimated by the three-state approximation, which assumes a single term dominates in the sum-over-states (SOS) in eq 2, and in the case where the two photons have the same energy (E_λ), the cross-section is given by

$$\delta_{f0}^I = \frac{32\pi^4 g_{max}}{15(ch)^2} \frac{E_\lambda^2}{(E_i - E_\lambda)^2} |\mu_{0i}|^2 |\mu_{if}|^2 (2\cos^2 \Theta_{\mu\mu} + 1) \quad (3)$$

where g_{max} is the maximum of the line width function, and $\Theta_{\mu\mu}$ is the angle between the two transition dipole moment vectors. While the three-state approximation is often not adequate for quantitative results, it can be useful in analyzing the origin of the TPA intensity, as we have previously shown.[34]

TPA has been calculated by the above formalism for a number of organic systems,[30,33,34,44-48] which generally only have a few states near the visible spectrum, and thus the SOS can be rapidly converged. The decay constant Γ_i in eq 2 makes a significant contribution only near resonance, i.e., when the photon energy is very close to a one-photon allowed state energy. In gold clusters, the density of states is much higher, and a near resonant condition is highly likely and generally dominates the TPA. This makes the inclusion of an appropriate decay constant in eq 2 more important in the calculation of TPA in gold clusters than in organic chromophores. The SOS method enables introduction of few-state models, which can be used with the calculation of transition dipole moments between excited states from the double residue of the response function. As described in the next session, the most computationally efficient method for calculation of the TPA is through the quadratic response single residue, and thus this method must be used for the larger clusters. However, in the single residue methodology the TPA probability is obtained directly without carrying out a SOS, so the damping factor is not a part of the formalism. However, a qualitative understanding was provided. Al-

Calculation of Absorption Spectra

J. Chem. Theory Comput., Vol. 6, No. 9, 2010 **2811**

though inorganic and hybrid structures have been previously applied in nonlinear optical applications,[49] the use of gold thiolate cluster compounds of high stability provides a platform for gaining a more fundamental understanding.

III. Computational Methods

The importance of including relativistic effects in calculations on gold has been well established.[50] In order to avoid the computational complexity of including relativistic effects through solution of the Dirac equation, approximations have been developed, such as the Douglas−Kroll (DK)[51,52] method, which is tested here in the GAMESS[53] and Dalton[54,55] programs, and the zero-order regular approximation (ZORA),[56,57] which is used in the ADF[58−60] program. The most computationally efficient method to include relativistic effects is through pseudopotentials. When using pseudopotentials, so-called effective core potentials (ECP), the core electrons are removed from the full calculation, and their effects are included through a simpler scaled method, greatly reducing the amount of computation. In addition, the relativistic effects can be included in the parametrization at almost no additional cost. Well parametrized pseudopotentials can be competitive in accuracy with the more expensive all-electron DK and ZORA methods. In order to check the effects of spin−orbit coupling, the two following methods were tested: the perturbative inclusion of spin−orbit coupling (PSOC)[61] and the relativistic spin−orbit ZORA (RSOZ)[62] (available in ADF).

For the isolated gold dimer, the experimental bond length of 2.472 Å[17] has been used in the TDDFT calculations. The molecular geometry for $[Au_2(SH)]^{-1}$ was optimized with the BP86[63,64] X-C functional and the improved model core potential with scaled relativistic effects (iMCP-SR2),[65] hereafter abbreviated SR2, and the corresponding basis set in the GAMESS[53] program. The geometry of $[Au_{25}(SR)_{18}]^{-1}$ for R = H was initially optimized with the ADF program at the BP86/ZORA/TZP level of theory with a frozen core of 4f for gold and 2p for sulfur. A recent study[26] indicated better agreement with the experimental structure when the exchange-only Xα functional was used in the geometry optimization, and therefore a second optimized geometry was obtained for this molecule using this functional, and both geometries were tested in TDDFT calculations. The Xα functional is the Slater[66] exchange functional with α = 0.7 and is equivalent to local density approximation (LDA) if correlation is ignored.

For use with the DK method, a basis set for gold has been developed from the general contractions of Tsuchiya et al.[67,68] and labeled "b41". This basis set is a 26s23p15d10f/11s10p7d3f contraction and is given in Table S1of the Supporting Information. Linear response TDDFT calculations were carried out with this basis set and the DK method, with DZP and TZP basis sets and the ZORA method, and with the SR2, LANL2DZ,[69] and SDD-DZ[70,71] pseudopotentials and corresponding basis sets. Since quadratic response TDDFT is available only in the Dalton[55] program, the TPA results are limited to the basis sets b41/DK, LANL2DZ, and SDD. Linear response TDDFT calculations were carried out with the generalized gradient approximation (GGA) func-

tional BP86, the hybrid functional B3LYP,[63,72−75] and the long-range corrected (LC) functionals CAMB3LYP,[76] mCAM,[33,48] and SAOP,[77] while the quadratic response calculations were limited to the X-C functionals BP86, B3LYP, CAMB3LYP, and mCAM. For the dimer systems, OPA were also obtained from high-level coupled cluster methods, including the completely renormalized equation-of-motion coupled cluster singles and doubles with perturbative triples (CR-EOMCCSD(T))[78−80] in GAMESS and the similar CCSDR(3)[81] method in Dalton. OPA extinction coefficients and TPA cross-sections were obtained from the calculated oscillator strengths and TPA probabilities, respectively, by fitting to Gaussian line width functions, as described previously.[32] The full-width at half-maximum (fwhm) used in the line width functions was 0.2 and 0.3 eV for OPA and TPA, respectively.

The TPA spectrum has been calculated with the Dalton[55] program, using both the double residue method to obtain the excited-state transition dipole moments for use in the SOS expression (eq 2) and the single residue method to directly obtain the TPA probability.[82−85] While the single residue method is more computationally efficient, the SOS method allows for the inclusion of the intermediate-state decay constant (also called the damping constant or broadening factor, Γ_i in eq 2). In the calculation of the TPA cross-section using quadratic response TDDFT, resonance effects can produce unphysically large TPA cross-sections, and this damping constant is needed to mitigate this problem. Combining calculated TPA cross-sections with classical laser pulse propogation simulations has been proposed by Agren et al.[86]

IV. Results

A. Au_2 and $[Au_2SH]^{-1}$. While the TDDFT calculations were carried out at the experimental geometry, geometry optimization of this smallest gold cluster was carried out with DFT to test several X-C functionals, including the hybrid B3LYP and the meta-hybrid M06.[87] The results are given in Table S2 in the Supporting Information. As was found for the Au_{25} system, exchange-only LDA functionals, such as Xα and Slater, give good agreement with the experimental geometry, while GGA X-C functionals, such as BP86, tend to overestimate the bond length, and the overestimation is even worse when the hybrid B3LYP functional is used. Including the empirical dispersion correction of Grimme[88] yields a small increase in the bond length, which slightly worsens the agreement with experiment.

The calculated OPA energies and oscillator strengths for Au_2 are given in Table 1 and compared to experiment, while the calculated values for Au_2SH^{-1} are given in Table 2. High-level theoretical results from CCSD(T) were also used to evaluate the TDDFT methods. Experimentally, the gold dimer is characterized by the A and B lines measured at 2.44 and 3.18 eV, respectively, with corresponding reported oscillator strengths of 0.05 and 0.13.[13,14] In most of the calculated results, the A line is considerably weaker than measured, while the B line is stronger than experiment, both of which may be due to the effects of vibronic coupling in

Table 1. OPA Excitation Energies and Oscillator Strengths for Au_2

functional	basis set	Π_u ΔE(eV)	Π_u f	Σ_u^+ ΔE(eV)	Σ_u^+ f
BP86	LANL2DZ	2.480	0.007	2.909	0.160
B3LYP	LANL2DZ	2.808	0.008	3.075	0.200
CAMB3LYP	LANL2DZ	2.989	0.010	3.115	0.211
mCAMB3LYP	LANL2DZ	2.883	0.009	3.093	0.206
BP86	SDD-DZ	2.363	0.007	2.850	0.128
B3LYP	SDD-DZ	2.703	0.008	2.992	0.170
CAMB3LYP	SDD-DZ	2.882	0.009	3.016	0.180
mCAMB3LYP	SDD-DZ	2.773	0.008	3.002	0.175
BP86	IMCP-SR2	2.655	0.007	2.929	0.152
B3LYP	IMCP-SR2	2.830	0.008	3.075	0.172
BP86	B41/DK	2.311	0.007	2.813	0.129
B3LYP	B41/DK	2.650	0.009	2.976	0.169
CAMB3LYP	B41/DK	2.848	0.011	3.023	0.182
mCAMB3LYP	B41/DK	2.723	0.009	2.993	0.174
BP86	DZ.4d/ZORA	2.734	0.008	3.011	0.147
BP86	DZ.4f/ZORA	2.726	0.008	3.009	0.149
BP86	TZP.4d/ZORA	2.426	0.007	2.867	0.132
BP86	TZP.4f/ZORA	2.416	0.007	2.863	0.133
SAOP	TZP/ZORA	2.886	0.008	3.096	0.166
SAOP-PSOC	TZP/ZORA	2.877	0.005	3.273	0.128
				2.344	0.041
SAOP-RSOZ	TZP/ZORA	2.900	0.005	3.304	0.156
				2.350	0.020
CR-EOMCCSD(T)	IMCP-SR2	2.968	0.012	2.895	0.274
CCSDR(3)	LANL2DZ	2.867	0.013	2.884	0.222
CCSDR(3)	SDD-DZ	2.733	0.012	2.764	0.199
experiment[13]		2.435	0.050	3.184	0.130

Table 2. OPA for Au_2SH^{-1}

functional	basis set	Π_u ΔE(eV)	Π_u f	Σ_u^+ ΔE(eV)	Σ_u^+ f
BP86	LANL2DZ	2.7287	0.0014	3.3176	0.1200
B3LYP	LANL2DZ	3.1101	0.0022	3.4351	0.1770
CAMB3LYP	LANL2DZ	3.5330	0.0015	3.4699	0.1853
mCAMB3LYP	LANL2DZ	3.2995	0.0020	3.4562	0.1843
BP86	SDD-DZ	2.5943	0.0007	3.0831	0.1082
B3LYP	SDD-DZ	2.9702	0.0014	3.2014	0.1597
CAMB3LYP	SDD-DZ	3.3783	0.0011	3.2432	0.1689
mCAMB3LYP	SDD-DZ	3.1531	0.0013	3.2249	0.1664
BP86	B41/DK	2.8541	0.0004	3.6725	0.1098
B3LYP	B41/DK	3.3159	0.0004	3.8978	0.1483
CAMB3LYP	B41/DK	3.7555	0.0000	3.9599	0.1595
mCAMB3LYP	B41/DK	3.5029	0.0002	3.9291	0.1536
BP86	ZORA/TZP.4f	2.6785	0.0014	3.3129	0.1276
SAOP	ZORA/TZP	3.0142	0.0027	3.6610	0.2293
CR-EOMCCSD(T)	IMCP-SR2	3.4450	0.0009	3.6980	0.2745
CCSDR(3)	LANL2DZ	3.2874	0.0015	3.4366	0.1403
CCSDR(3)	SDD-DZ	3.1951	0.0010	3.3431	0.1297

the measured absorption spectra, an effect not included in the calculations. Another possible explanation is spin−orbit coupling, which will be discussed in the next paragraph. Thus, the comparison to the CCSD(T) results may be more useful for evaluation of the X-C functionals. Also, while experimental results are not available for $[Au_2SH]^{-1}$, the performance of the X-C functionals on this simple gold thiolate can also be evaluated by comparison to CCSD(T) results. As in a previous TDDFT study by Wang et al.,[23] the A line in the gold dimer was assigned to the excitation to the first Π_u state, while the stronger B line was assigned to the transition to the first Σ_u^+ state. The calculated A line, in addition to being considerably weaker than experiment,

is blue-shifted by 0.3 to 0.5 eV, while the calculated B line is red-shifted compared to experiment by 0.2 to 0.4 eV. As a result, in the calculated results, the two states are nearly accidentally degenerate and would not be distinguishable as separate absorption lines. For example, at the highest theoretical level carried out, CCSD(T), the difference in energy of these two final states is only about 0.02 eV (Table 1). The TDDFT results using the CAMB3LYP and mCAM functionals are in the best agreement with CCSD(T) for Au_2, yielding excitation energies with less than 0.1 eV error for the A line and 0.1 to 0.2 eV for the B line. The oscillator strengths calculated using these two functionals are only slightly smaller than the CCSD(T) values, and the calculated split between the A and B line is about 0.2 eV. The results using the B3LYP and SAOP functionals are also in good agreement with the CCSD(T) values, while for the BP86 functional the agreement is not as good. To test the possibility that the discrepancy between the calculated and measured linear absorption spectra is due to the effects of spin−orbit coupling, linear TDDFT calculations were carried out using the relativistic spin−orbit ZORA (RSOZ)[62] and the more computationally efficient perturbative inclusion of spin−orbit coupling (PSOC).[61] The results of these calculations, carried out with the SAOP X-C functional, are also included in Table 1. The difference is the existence of another Σ_u^+ state, at an excitation energy of 2.3 eV, which appears in both of these calculations. The calculated oscillator strength and excitation energy of this state is in much better agreement with the measured A line than the calculated Π_u state. Furthermore, the calculated oscillator strength of the transition to the Σ_u^+ state near 3.2 eV was reduced, making it in better agreement with the measured B line. Thus, explicit inclusion of spin−orbit coupling effects by one of these methods is recommended for Au_2. The RSOZ and PSOC methods were also tested on the $Au_{25}(SH)_{18}^{-1}$ and $Au_{12}(SH)_9^{+1}$ systems, but the effects on the calculated spectra were small. Thus, these methods are not included in the results given for these systems. The first geometry considered for $[Au_2(SH)]^{-1}$ was a bridged C_{2v} structure with the thiolate bonded to both gold atoms. This was found to be a saddle point, and instead the minimum-energy structure was found to have the sulfur atom bonded to just one of the gold atoms, nearly collinear with the two gold atoms. The optimized geometry has the following bond lengths in Å (compared to the experimental value for Au_2 of 2.472): Au−Au = 2.5803, Au−S = 2.3054, and S−H = 1.3538; and bond-angles in degrees (°): Au−Au−S = 179.3 and Au−S−H = 95.8. The molecule is nearly planar with the dihedral angle Au−Au−S−H equal to 173.3°. The effect of thiolation on the absorption spectrum of the gold dimer, as calculated at the CCSD(T) level, is to blue-shift the A line by 0.45 eV and decrease its intensity by a factor of 10 and to blue-shift the B line by 0.55 eV and decrease its intensity by nearly a factor of 2. The TDDFT results using the CAMB3LYP and mCAM functionals with pseudopotentials are in good agreement with the CCSD(T) results.

The TPA cross-sections calculated for the gold dimer with the different X-C functionals are not as consistent as the OPA spectra. The TPA results for Au_2 are given in Table 3. The

Calculation of Absorption Spectra

J. Chem. Theory Comput., Vol. 6, No. 9, 2010 **2813**

Table 3. TPA for Au_2[a]

functional	basis set	ΔE (eV)	σ_2 (GM)	$\mu_{01}{}^2$	$\mu_{12}{}^2$	R	E_1 (eV)
BP86	LANL2DZ	6.200	1.500×10^4	1.45×10^1	1.36×10^2	1.03×10^3	2.91
B3LYP	LANL2DZ	6.260	1.654×10^6	1.71×10^1	9.40×10^2	1.34×10^4	3.08
CAMB3LYP	LANL2DZ	6.420	1.387×10^5	1.79×10^1	2.16×10^2	4.72×10^3	3.11
mCAMB3LYP	LANL2DZ	6.315	7.398×10^5	1.76×10^1	5.72×10^2	9.57×10^3	3.09
BP86	SDD-DZ	6.027	1.577×10^4	1.19×10^1	1.28×10^2	1.36×10^3	2.85
B3LYP	SDD-DZ	5.983	1.548×10^{13}	1.50×10^1	2.23×10^6	5.59×10^7	2.99
CAMB3LYP	SDD-DZ	6.127	8.237×10^5	1.57×10^1	4.02×10^2	1.71×10^4	3.02
mCAMB3LYP	SDD-DZ	6.032	1.118×10^8	1.54×10^1	5.44×10^3	1.74×10^5	3.00
BP86	B41/DK	7.100	2.230×10^2	1.21×10^1	2.21×10^1	9.25×10^1	2.81
B3LYP	B41/DK	7.265	4.610×10^2	1.50×10^1	3.11×10^1	1.23×10^2	2.98
CAMB3LYP	B41/DK	7.390	3.585×10^2	1.59×10^1	2.40×10^1	1.21×10^2	3.02
mCAMB3LYP	B41/DK	7.315	4.267×10^2	1.54×10^1	5.35×10^1	1.21×10^2	2.99

[a] Including the transition energy (ΔE), the TPA cross-section (σ_2), the squares of the most relevant transition dipole moments (μ), the resonance enhancement factor (R), and the intermediate-state excitation energy (E_1).

calculations using the DK approximation yield the smallest and most realistic TPA cross-sections, ranging from 223 to 461 GM, while the largest cross-sections are obtained using the SDD-DZ pseudopotential, ranging from 10^4 to 10^{13} GM. While each TPA cross-section reported in Table 3 was obtained from the residue of the quadratic response function and is thus equivalent to the full SOS approximation, also listed are the transition dipole moments and resonance enhancement factors (R), which can be used in the three-state approximation. As the three-state approximation yields a good prediction for this system, these values indicate the source of the variation in the calculated TPA. When SDD is used, the two-photon state is about 6 eV above the ground state, and since the strong OPA state is near 3 eV, R is large. Since the energy of the TPA state in the DK calculations is about 7.2 eV, R is much smaller. Also, in Figure S1 in the Supporting Information, the square of each relevant excited-state transition dipole moment obtained in a quadratic response calculation is plotted against the resonance enhancement factor, and there appears to be a correlation. Methods which have a large value for the resonance enhancement factor also have a large value for the excited-state transition dipole moment, indicating a relationship in these quantities. The TPA data for $[Au_2(SH)]^{-1}$ is given in Table S3 in the Supporting Information. Some of the same trends are observed, with the DK method yielding the smallest peak cross-sections (1500−475 000 GM) and the SDD pseudopotential yielding the largest (10^7−10^{16} GM). However, the reduction in symmetry for this compound increases the density of allowed states and opens more possibilities for highly resonant terms. As a result, the calculated peak TPA cross-section occurs over a range of transition energies from 6.68−7.05 eV for LANL2DZ, from 6.40−8.99 eV for SDD-DZ, and from 7.76−8.03 eV for the DK method. In the SOS method, the OPA decay constant broadens the intermediate state and thus dampens the TPA near the resonance, yielding a more physically realistic TPA cross-section.

B. $Au_{25}(SH)_{18}{}^{-1}$. *1. OPA*. In Table 4, the calculated linear absorption spectrum for $Au_{25}(SH)_{18}{}^{-1}$ is compared to the measured spectra of Negishi et al.,[27,28] Ramakrishna et al.,[2,4] and Zhu et al.[3] Four absorption peaks, labeled a−d, were identified from the spectrum of Negishi et al.,[27] including absolute extinction coefficients based on the value of 8800

$M^{-1}cm^{-1}$ at 670 nm (1.85 eV). Zhu et al.[3] identified the first three peaks in excellent agreement with Negishi et al.,[27] although no absolute intensities were given. The extinction coefficients in the spectrum of Ramakrishna et al.[2] were scaled by 0.1 to be consistent with the intensities of Negishi et al.,[27] and the four peaks are identified in good agreement with Negishi et al.[27] As was found by Aikens,[26] the calculated spectrum for $Au_{25}(SH)_{18}{}^{-1}$ is in best agreement with experiment when the geometry optimized with the LDA exchange-only functional $X\alpha$ is used. When the geometry optimized with the GGA (BP86) X-C functional was used in the linear response calculations, the average deviation from the experimental excitation energies was larger than when the geometry optimized with $X\alpha$ was used, and this can be explained by comparison with the experimental geometry of the Au_{13} icosahedral core. The average distance of the iscosahedral vertex Au atoms from the central Au atom is about 2.78 Å in both the experimental and $X\alpha$ geometries, while it is 2.85 Å in the BP86 geometry. Geometry optimization was also carried out with the $X\alpha$ functional and the dispersion model of Grimme, but this caused considerable distortion in the core and raised the average distance to 2.84 Å.

A number of combinations of X-C functionals and basis sets have been used in linear response calculations with these two geometries, as given in Table 4. The spectrum obtained using the B3LYP X-C functional with the SDD basis set on the $X\alpha$ optimized geometry gives the best agreement with experiment, while using the mCAM functional with this basis and geometry also yields excellent agreement. The results using B3LYP, mCAM, and CAMB3LYP with the BP86 optimized geometry are also in good agreement with experiment. When TDDFT is carried out using the BP86 and SAOP X-C functionals, the excitation energy for the first peak is underestimated, but agreement is fair for the other peaks.

Table 5 lists the Kohn−Sham orbital gaps for the relevant transitions and the corresponding linear response excitation energy for the SAOP, B3LYP, and mCAM functionals at the two geometries. As pointed out previously by Akola et al.[6] and Aikens,[89] in the super-atom model this system has an occupation of $1S^2 1P^6 1D^0 2S^0...$, so the highest occupied molecular orbital (HOMO) is an approximate triply degenerate 1P (Figure S2 in the Supporting Information), while the expected quintuply degenerate 1D is split by the octahedral

Table 4. OPA Excitation Energies and Extinction Coefficient Maxima for $Au_{25}(SR)_{18}^{-1}$ with Various X-C Functionals, Basis Sets, and Geometries[a]

TDDFT	geometry		peaks				
			a	b	c	d	
measured[27,28]		ΔE(eV)	1.851	2.755	3.092	3.780	
		ε_{max}	8.80×10^3	2.70×10^4	3.34×10^4	6.52×10^4	
measured[2,4]		ΔE(eV)	1.834	2.878	3.166	3.727	
(scaled by $\times$ 0.1)		ε_{max}	9.43×10^3	3.08×10^4	3.76×10^4	5.56×10^4	
measured[3]		ΔE(eV)	1.800	2.750	3.100		
BP86/ZORA	BP86	ΔE(eV)	1.408	2.573	3.393	3.883	4.163
		ε_{max}	8.91×10^3	4.16×10^4	3.27×10^4	5.92×10^4	6.24×10^4
SAOP/ZORA	BP86	ΔE(eV)	1.501	2.611	2.896	3.301	4.186
		ε_{max}	1.08×10^4	3.42×10^4	3.03×10^4	1.05×10^4	7.15×10^4
BP86/LANLDZ	BP86	ΔE(eV)	1.468	2.678	3.193		
		ε_{max}	9.29×10^3	4.41×10^4	7.52×10^3		
B3LYP/LANLDZ	BP86	ΔE(eV)	1.763	3.013	2.818	3.333	4.043
		ε_{max}	1.54×10^4	3.38×10^4	1.98×10^4	5.48×10^4	2.38×10^4
mCAM/LANLDZ	BP86	ΔE(eV)	1.881	3.056	3.311	3.626	4.411
		ε_{max}	1.79×10^4	3.01×10^4	3.10×10^4	7.07×10^4	3.92×10^4
BP86/SDD-DZ	BP86	ΔE(eV)	1.448	2.613	3.278		
		ε_{max}	9.24×10^3	4.04×10^4	9.33×10^3		
B3LYP/SDD-DZ	BP86	ΔE(eV)	1.754	2.949	2.819	3.274	3.994
		ε_{max}	1.55×10^4	3.09×10^4	2.64×10^4	5.28×10^4	2.48×10^4
mCAM/SDD-DZ	BP86	ΔE(eV)	1.876	2.991	3.29	3.561	4.306
		ε_{max}	1.79×10^4	3.05×10^4	2.92×10^4	6.87×10^4	3.69×10^4
CAMB3LYP/SDD-DZ	BP86	ΔE(eV)	2.048	2.863	3.238	3.948	4.723
		ε_{max}	2.08×10^4	3.50×10^3	4.39×10^4	9.73×10^4	6.51×10^4
SAOP/ZORA	Xα	ΔE(eV)	1.602	2.592	2.937	3.522	
		ε_{max}	1.14×10^4	2.82×10^4	2.38×10^4	2.68×10^4	
B3LYP/LANLDZ	Xα	ΔE(eV)	1.861	2.881	2.956	3.381	4.051
		ε_{max}	1.58×10^4	2.60×10^4	2.52×10^4	4.74×10^4	3.89×10^4
B3LYP/SDD-DZ	Xα	ΔE(eV)	1.844	2.754	2.954	3.324	3.929
		ε_{max}	1.57×10^4	2.47×10^4	2.02×10^4	4.38×10^4	4.07×10^4
mCAM/SDD-DZ	Xα	ΔE(eV)	1.958	2.928	3.258	3.593	4.193
		ε_{max}	1.81×10^4	3.35×10^4	1.92×10^4	5.94×10^4	5.72×10^4

[a] Geometry optimizations were carried out with the ZORA/TZP basis set.

Table 5. Calculated Kohn–Sham Orbital Differences (eV) and Corresponding Peaks in the TDDFT Linear Response Spectrum of $Au_{25}(SR)_{18}^{-1}$[a]

TDDFT	geometry		$1P \rightarrow 1D_{zz}$		$1P \rightarrow 1D_{xy}$	$1P \rightarrow 2S$	
			H → L	H-2 → L	H → L+1	H → L+2	H-5 → L
SAOP/TZP[3]	BP86/TZP	K–S gap (eV)	1.37	2.42	2.31	2.52	
		linear response	1.52		2.63		2.91
SAOP/TZP[94]	Xα/TZP	K–S gap (eV)	1.48	2.42	2.30	2.73[b]	
		linear response	1.63	2.48	2.59	2.77[b]	2.97
SAOP/TZP	BP86/TZP	K–S gap (eV)	1.34	2.42	2.31	2.43	2.81
		linear response	1.50	2.48	2.61	2.52	2.90
SAOP/TZP	Xα/TZP	K–S gap (eV)	1.46	2.42	2.31	2.64[b]	2.86
		linear response	1.60	2.49	2.59	2.63[b]	2.94
B3LYP/SDD	BP86/TZP	K–S gap (eV)	2.24	3.53	3.23		3.82
		linear response	1.75	2.95	2.82	2.77	3.27
B3LYP/SDD	Xα/TZP	K–S gap (eV)	2.34	3.55	3.20		3.87
		linear response	1.84	2.95	2.75	3.04	3.32
mCAM/SDD	Xα/TZP	K–S gap (eV)	3.05	4.39	3.97		4.72
		linear response	1.96	3.26	2.93	2.33	3.59
		expt[3]	1.80		2.75		3.10

[a] The experimental peaks are also listed for comparison. [b] The final state is L+3 in this calculation.

field of the six ligand wings into an approximately doubly degenerate lowest unoccupied molecular orbital (LUMO) (D_z^2, $D_{x^2-y^2}$; Figure S3 in the Supporting Information) and triply degenerate LUMO+1 (D_{xy}, D_{yz}, D_{xz}, Figure S4 in the Supporting Information). While the HOMO-1 should thus be the nondegenerate 1S, the HOMO-1 is, in fact, approximately doubly degenerate due to mixing between the ligand orbitals and the valence d orbitals of the icosohedral gold core, and furthermore, the HOMO-1 (Figure S5 in the

Supporting Information) does not have super-atom 1S character, which was shown previously by Akola et al.[6] Due to mixing in the sub-HOMO orbitals, a super-atom 1S orbital is difficult to identify but may be the HOMO-6 orbital. From the angular momentum selection rule $\Delta L = \pm 1$, the spectrum is expected to be dominated by transitions from the 1P HOMO to the 1D LUMO or LUMO+1 or to the 2S, which is the LUMO+2 in all the hybrid calculations and in the SAOP//BP86 calculation, and is the LUMO+3 in the

Calculation of Absorption Spectra

J. Chem. Theory Comput., Vol. 6, No. 9, 2010 **2815**
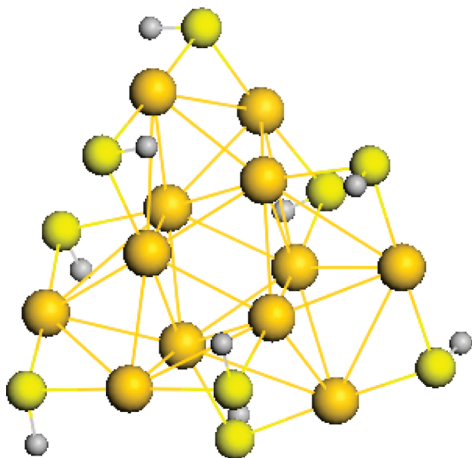
**Figure 2.** Structure for $Au_{12}(SH)_9^{+1}$.

SAOP//Xα calculation.[89] In addition, while the system does not have exact D_{2h} symmetry, C_i symmetry was enforced so only transitions that change parity are dipole allowed. The HOMO has a_u symmetry, and the LUMO, LUMO+1, and LUMO+2 (or LUMO+3 for SAOP// Xα) are all a_g symmetry, so these transitions are all allowed. The HOMO-2, HOMO-5, and HOMO-7 (all triply degenerate) all have, like the HOMO, a_u symmetry so could also be involved in transitions to the low lying unoccupied orbitals, while HOMO-1, HOMO-3, HOMO-4, and HOMO-6 are a_g symmetry and thus are unlikely to be involved in the OPA spectrum. The SAOP, B3LYP, CAM, and mCAM were designed to correct for the asymptotic deficiencies of GGA functionals, such as BP86, but only the functionals that include exact exchange (B3LYP, CAM, and mCAM) yield significantly different HOMO−LUMO gaps (2.2−4.0 eV) than the BP86 gap of 1.30 eV, while the SAOP functional only increases the gap slightly compared to BP86. For these X-C functionals, the first peak in the spectrum (peak a) is due to HOMO → LUMO transitions, but the linear response behavior of the hybrid functionals is significantly different from that of the nonhybrid functionals. In the SAOP calculations, the HOMO−LUMO gap of 1.48 eV is about 0.3 eV less than the corresponding experimental excitation energy, and linear response theory provides a small positive correction to produce a first peak at 1.63 eV, still about 0.2 eV below the experimental value. In the B3LYP calculation, the HOMO−LUMO gap is about 0.5 eV above the measured excitation energy, while in this linear response calculation, the negative contribution from the exact exchange component places the first peak in nearly exact agreement with experiment.

Peak b is dominated by HOMO → LUMO+1 transitions in all the calculations. However, in the SAOP calculations, peak b also gets significant contributions from excited states dominated by HOMO-2 → LUMO and HOMO → LUMO+2 (or LUMO+3) transitions, while in the hybrid calculations, the excited states from these transitions are higher in energy and produce peak c. In the SAOP calculations, peak c is primarily from HOMO-5 → LUMO transitions, while in the hybrid calculations, these transitions produce peak d.

2. TPA. The TPA for $Au_{25}(SH)_{18}^{-1}$ was calculated using the BP86, B3LYP, and mCAM functionals with the LANL2DZ and SDD-DZ basis sets. The transition energies and the calculated TPA cross-sections are listed in Table S5 in the Supporting Information. As with the gold dimer systems, the high density of states makes resonance effects problematic, and a wide variation in peak TPA cross-sections is obtained. For each level of theory, the largest TPA cross-sections benefit from resonant enhancement from the first excited state, and the overall transition is

$$HOMO \rightarrow LUMO + n$$

Where $n = 3−6$. In the super-atom theory, these final states are all 1F orbitals. As can be seen in the SOS expression, eq 2, TPA requires an intermediate state that has dipole-allowed transitions with both the initial and final states. Thus, with the excited states responsible for peak a in the OPA spectrum (which correspond to HOMO → LUMO transitions) acting as the intermediate or "virtual" state in the TPA process, the TPA can be written like the analogous two-step OPA process:

$$HOMO(1P) \rightarrow LUMO(1D) \rightarrow LUMO + n(1F)$$
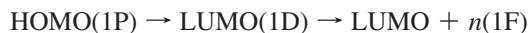
thus obeying the $\Delta L = \pm 1$ rule for each step. As expected from this rule, transitions from the HOMO (1P) to the 1F orbitals were forbidden in OPA but are the strong TPA states. The B3LYP/SDD-DZ results include two TPA states with nearly the same transition energy as experiment, one of which (at 3.17 eV) has a TPA cross-section (620 000 GM) of a similar magnitude as experiment, while the other is significantly larger.

While the B3LYP/SDD-DZ calculation produced a number of measurable TPA transitions in the range of 3−4 eV, the calculated TPA to the states near 1.9 eV is very small. This is expected as these states are all A_u in the C_i symmetry of this molecule, and the selection rules require that TPA states be of A_g symmetry. While the experimental results include a TPA cross-section of 2700 GM at 1.92 eV, the experimental results are not TPA maxima but are measurements of TPA at the individual wavelengths of 1290 and 800 nm, corresponding to TPA transition energies of 1.92 and 3.10 eV. In the calculated TPA results reported here, a line width of 0.3 eV (fwhm) was used to allow for resolution of the different states, but the actual line width is unknown. Both experiment and our calculations indicate a large TPA peak of greater than 10^5 GM near a transition energy of 3.1 eV, and by using a line width in the range 0.5 to 1.0 eV, the tail of this large absorption band would extend to 1.9 eV, and the calculated TPA cross-section at this energy would be similar in magnitude to the reported experimental value. Thus, without some knowledge of the broadening factors for this system, only qualitative predictions of TPA can be calculated.

C. $Au_{12}(SR)_9^{+1}$. The stability of thiolated gold clusters that obey the shell-filling super-atom theory, such as $Au_{25}(SH)_{18}^{-1}$ for $n^* = 8$ and $Au_{102}(SH)_{44}$ for $n^* = 58$, motivated a search for super-atom clusters with $n^* = 2$, and two structures were proposed.[24] While it was previously proposed[90] that the smallest thiolated gold clusters may be

Table 6. Calculated Au−Au Bondlengths in $Au_{12}(SR)_9^{+1}$ (Å) as well as Average Deviation from the Previously Calculated Geometry[24]

R =	H BP86/SR2	H Xα/ZORA	H TPSS/ZORA	H B3LYP/ZORA	CH_3 Xα/ZORA	CH_3 TPSS/ZORA	CH_3 TPSS[24]
Core							
1,2	2.882	2.837	2.776	2.881	2.867	2.872	2.875
2,3	2.882	2.837	2.776	2.881	2.866	2.872	2.875
1,3	2.882	2.837	2.776	2.881	2.867	2.874	2.875
4,5	2.882	2.837	2.776	2.881	2.868	2.865	2.875
5,6	2.882	2.837	2.776	2.881	2.869	2.864	2.875
4,6	2.882	2.837	2.776	2.881	2.866	2.861	2.875
1,4	2.821	2.758	2.944	3.027	2.745	2.793	2.813
1,6	2.748	2.715	2.921	2.852	2.709	2.745	2.760
2,4	2.748	2.715	2.921	2.852	2.710	2.746	2.760
2,5	2.821	2.758	2.944	3.027	2.744	2.795	2.813
3,5	2.748	2.715	2.921	2.852	2.709	2.745	2.760
3,6	2.821	2.758	2.944	3.027	2.745	2.792	2.813
av	2.833	2.787	2.854	2.910	2.797	2.819	2.831
av dev.	0.008	0.044	0.123	0.079	0.034	0.012	
Wings							
2,12	2.893	2.838	3.019	3.137	2.798	2.864	2.876
5,12	3.062	3.069	3.009	3.263	2.953	3.001	3.012
2,9	3.083	3.069	3.009	3.263	2.992	3.083	3.052
5,9	2.873	2.838	3.019	3.137	2.778	2.826	2.852
1,11	2.893	2.838	3.019	3.137	2.798	2.864	2.876
1,8	3.083	3.069	3.009	3.263	2.994	3.085	3.052
4,11	3.062	3.069	3.009	3.263	2.954	3.001	3.012
4,8	2.873	2.838	3.019	3.137	2.777	2.826	2.852
3,7	3.083	3.069	3.009	3.263	2.992	3.084	3.052
3,10	2.893	2.838	3.019	3.137	2.797	2.865	2.876
6,7	2.873	2.838	3.019	3.137	2.777	2.823	2.852
6,10	3.062	3.069	3.009	3.263	2.954	3.005	3.012
av	2.978	2.954	3.014	3.200	2.880	2.944	2.948
av dev.	0.030	0.031	0.089	0.252	0.068	0.020	

protected by $SR(AuSR)_3$ (trimer) wings due to the need for this longer ligand to wrap around the smaller core, both structures use the dimer wings as in $Au_{25}(SH)_{18}^{-1}$. The first proposed structure, $Au_8(SR)_6$, has a tetrahedral Au_4 core and two $SR(AuSR)_2$ wings. However, the optimized structure left the core exposed and was rejected as probably unstable.[24] The second proposed structure, $Au_{12}(SR)_9^{+1}$, has an Au_6 octahedral core and three $SR(AuSR)_2$ wings and has approximate C_3 symmetry (see Figure 2). Jiang et al[24] optimized the geometry for this structure with R = Me using the TPSS[91] X-C functional and evaluated the OPA using the PBE[92] functional. The geometry for this system has been optimized in this study for R = H with BP86/SR2, Xα/ZORA, and B3LYP/ZORA and for R = CH_3 with Xα/ZORA and TPSS/ZORA, and the core bond lengths for each level of theory are given in Table 6. As with the Au_{25} cluster, shorter bondlengths are obtained in the gold core when the Xα X-C functional is used in the optimization compared to the results with either the BP86 or the TPSS functionals. In the Au_{25} cluster, the Xα geometry was in better agreement with the experimental geometry than the GGA geometries, and using the Xα geometry in the TDDFT calculation produced a spectrum in better agreement with the experimental spectrum. While a compound with the formula $Au_{12}(SR)_9$ has been identified in a study of polydispersed gold nanoclusters,[93] no experimental data on the structure is available for comparison. Thus, multiple geometries and functionals have been tested in the TDDFT calculations.

The excitation energy, oscillator strength, and primary orbital transition for each peak in the calculated OPA spectrum for $Au_{12}(SR)_9^{+1}$ is listed in Table 7. The superatom theory can also be used for this system to a limited extent. With $n^* = 2$, the HOMO is the nondegenerate 1S, and the LUMO should be the triply degenerate 1P. However, ligand field splitting from the C_3 symmetry splits the 1P orbitals into a doubly degenerate LUMO and a nondegenerate LUMO+1. As expected, the first peak in the spectrum is due to HOMO → LUMO transitions. Similar to the results from the Au_{25} cluster, when the hybrid functional B3LYP is used, the HOMO−LUMO gap is much larger (by about 1 eV) than when one of the nonhybrid GGA functionals is used, and the first peak in the linear response spectrum is blue-shifted by about 0.3 eV and has nearly twice the peak intensity. Both the blue-shift and intensity increase are even larger when mCAM is used.

For the higher states, the geometry used plays a major role. For the R = H system, when the BP86 geometry is used, the HOMO-1 → HOMO gap is large (0.70, 0.97, and 1.08 eV for the PBE, B3LYP, and mCAM results, respectively), while the LUMO → LUMO+1 gap is smaller (0.55, 0.59, and 0.63 eV). When the Xα geometry is used, these gaps are reversed; the HOMO-1 → HOMO gap is small (0.33, 0.59, and 0.77 eV), while the LUMO → LUMO+1 gap is large (0.95, 1.01, and 1.04 eV). Thus, while the calculations with the BP86 geometry show a weak but distinct second peak at about 2.8 eV from the HOMO →

Table 7. Calculated Absorption Peaks for $Au_{12}(SR)_9^{+1}$ as well as the Dominant Orbital Transition and Corresponding Kohn−Sham gap (eV)[a]

TDDFT	geometry						H-1 → H	L → L+1
R = Me								
PBE/tpz	TPSS	ΔE	1.811	2.536	3.016	3.651		
		ε_{max}	8.33×10^3	1.96×10^4	1.56×10^4	1.74×10^4		
			H → L	H-2 → L	H-5 → L			
		K−S gap	1.645	2.337			0.612	0.516
PBE/sdd	TPSS	ΔE	1.851	2.556	3.086	3.666		
		ε_{max}	9.36×10^3	2.03×10^4	1.85×10^4	1.71×10^4		
			H → L	H-2 → L	H-2 → L+1			
		K−S gap	1.672	2.405	2.944		0.607	0.539
mCAM/sdd	Xα	ΔE	2.254	3.319	4.204			
		ε_{max}	2.03×10^4	4.21×10^4	3.56×10^4			
			H → L	H-2 → L	H-3 → L+1			
		K−S gap	3.415	4.536	5.416		1.050	0.811
R = H								
PBE/sdd	BP86	ΔE	1.975	2.790	3.330	4.015		
		ε_{max}	1.03×10^4	2.30×10^4	2.31×10^4	2.03×10^4		
			H → L	H-1 → L	H-3 → L+1	H-7 → L+1		
		K−S gap	1.778	2.480	3.164	3.937	0.702	0.546
PBE/sdd	Xα	ΔE	1.916	2.711	2.981	3.606		
		ε_{max}	7.58×10^3	1.36×10^4	1.35×10^4	1.42×10^4		
			H → L	H-3 → L	H-4 → L	H-3 → L+1		
		K−S gap	1.715	2.541	2.877	3.828	0.327	0.951
B3LYP/sdd	BP86	ΔE	2.273	2.803	3.278	3.893		
		ε_{max}	1.75×10^4	4.54×10^3	3.82×10^4	3.55×10^4		
			H → L	H → L+1	H-2 → L	H-2 → L+1		
		K−S gap	2.797	3.391	3.883	4.477	0.966	0.594
B3LYP/sdd	Xα	ΔE	2.225	3.250	4.175	4.390		
		ε_{max}	1.49×10^4	2.78×10^4	2.44×10^4	2.37×10^4		
			H → L	H-4 → L	H-4 → L+1	H → L+5		
		K−S gap	2.756	3.865	4.872		0.592	1.007
mCAM/sdd	BP86	ΔE	2.408	2.953	3.483	4.158		
		ε_{max}	2.16×10^4	6.03×10^3	4.33×10^4	3.70×10^4		
			H → L	H → L+1	H-2 → L			
		K−S gap	3.583	4.213	4.774		1.078	0.630
mCAM/sdd	Xα	ΔE	2.377	2.877	3.447	3.852		
		ε_{max}	1.87×10^4	1.83×10^3	3.23×10^4	6.77×10^3		
			H → L	H-1 → L	H-4 → L	H-5 → L		
		K−S gap	3.555	4.322	4.901	5.129	0.767	1.039

[a] Excitation energy in eV and extinction coefficient in liter/cm/mol.

LUMO+1 transition, when the Xα geometry is used, the LUMO+1 orbital is too high in energy, and this peak is not found. In these calculations, HOMO-1 → LUMO transitions produce a weak shoulder on the next strong peak, which is dominated by transitions from HOMO-3 or HOMO-4 to the LUMO. Surprisingly, in both geometries, the LUMO+1 orbital is the $1P_z$ in the super-atom model, where the Z-axis is in the direction of the two unprotected faces in the octohedral core (perpendicular to the plane of the paper in Figure 2). In the more compressed Xα geometry, the $1P_x$ and $1P_y$ LUMO orbitals are slightly stabilized due to more interaction with the ligands, while the $1P_z$ LUMO+1 is slightly destabilized, resulting in the larger LUMO → LUMO+1 gap. The Xα geometry is also less spherically symmetric, which could also produce the greater deviation from the ideal super-atom model.

The use of a hybrid functional in the linear response calculation blue-shifts each of the major peaks relative to that obtained with a GGA functional. Using the Xα geometry seems to slightly red-shift the lines and reduce the intensity relative to the BP86 geometry for both the B3LYP and mCAM functional. Using the methyl ligand instead of
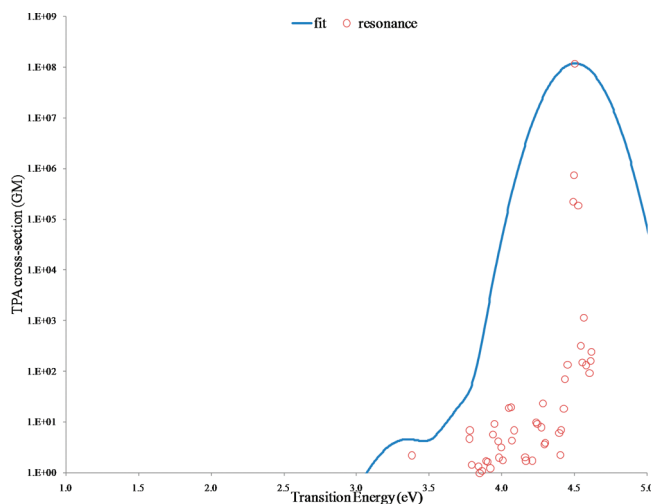
Figure 3. TPA for $Au_{12}(SCH_3)_9^{+1}$ using mCAM/SDD//Xα.

hydrogen also causes a red-shift but increases the intensity. The density of states is quite high above 3 eV.

Figure 3 shows the calculated two-photon absorption using mCAM/SDD-DZ//Xα. A Gaussian line shape was used with fwhm = 0.3 eV. The TPA seems to be dominated by

resonance effects from the first linear absorption line at 2.25 eV, resulting in a very large TPA at 4.5 eV. Due to the high density of states, several states have energies very close to resonance, including one at 4.501 eV with a TPA cross-section of 10^8 GM and three other states with TPA cross-sections greater than 10^5 GM. Compared to the TPA cross-sections calculated for the $Au_{25}(SH)_{18}{}^{-1}$ cluster, the smaller $Au_{12}(SR)_9{}^{+1}$ cluster has a smaller peak cross-section at a higher transition energy (for a given level of theory), which is consistent with the cluster-size scaling seen in the measured TPA cross-sections.[2,4] No significant off-resonant TPA was found for $Au_{12}(SR)_9{}^{+1}$.

V. Conclusions

The linear absorption spectrum has been calculated for the gold dimer and the monothiolated gold dimer anion using both time-dependent density functional theory (TDDFT) and the high-level completely renormalized equation-of-motion coupled cluster singles and doubles with perturbative triples (CR-EOMCCSD(T)) method. The CAMB3LYP and mCAM X-C functionals were found to give the best agreement with the high level of theory. The agreement between theory and experiment is not as good except when spin−orbit coupling effects are included in the calculations.

The calculated excitation energies of $Au_{25}(SH)_{18}{}^-$ are in excellent agreement with experiment when the Xα-optimized geometry is used with the B3LYP exchange−correlation (X-C) functional. Good agreement was also obtained with this geometry and the mCAM functional, and fair agreement was obtained when the BP86-optimized geometry was used with either the B3LYP, mCAM, or CAMB3LYP functional. The agreement was not as good when TDDFT was carried out with the BP86 functional, showing the importance of the asymptotic correction provided by the fraction of exact exchange in the hybrid functional. However, the systematic improvement in functionals that is required for achieving geometry optimization is still unclear.

The X-C functional used to optimize the geometry has a major effect on the calculated one-photon absorption (OPA) spectrum of $Au_{12}(SR)_9{}^{+1}$. The more compressed and less-symmetric Xα geometry increases the deviations from the super-atom model and significantly changes the calculated OPA spectrum, relative to the results using the BP86 X-C functional. This is in contrast to the $Au_{25}(SR)_{18}{}^{-1}$ results, where use of this functional only compressed the gold core without a loss of spherical symmetry. The inclusion of exact exchange in the response calculation also has a significant effect on the $Au_{12}(SR)_9{}^{+1}$ spectra.

For both $Au_{25}(SH)_{18}{}^{-1}$ and $Au_{12}(SR)_9{}^{+1}$, two-photon absorption (TPA) is dominated by resonance effects. The off-resonance TPA appears to be small. The large measured[4] TPA for $Au_{25}(SH)_{18}{}^{-1}$ of over 400 000 GM near a transition energy of 3.1 eV can be qualitatively explained by some of the calculated peaks, particularly when the B3LYP functional was used. However, the measured TPA of 2700 GM at a transition energy of 1.9 eV was not evident, although it could be the tail of the peak at 3.1 eV. Comparing the calculations on the clusters with 12 and 25 gold atoms, the smaller cluster has the smaller peak TPA cross-section at a higher transition

energy, as expected.[4] This understanding could motivate ligand substitution with moieties that are known to exhibit large two-photon absorption.

Supporting Information Available: In addition to the data already mentioned, the geometries used in this study are given in Table S5. This information is available free of charge via the Internet at http://pubs.acs.org.

References

(1) Jadzinsky, P. D.; Calero, G.; Ackerson, C. J.; Bushnell, D. A.; Kornberg, R. D. Structure of a Thiol Monolayer-Protected Gold Nanoparticle at 1.1 Å Resolution. *Science* **2007**, *318*, 430.

(2) Ramakrishna, G.; Varnavski, O.; Kim, J.; Lee, D.; Goodson, T. Quantum-Sized Gold Clusters as Efficient Two-Photon Absorbers. *J. Am. Chem. Soc.* **2008**, *130*, 5032.

(3) Zhu, M.; Aikens, C. M.; Hollander, F. J.; Schatz, G. C.; Jin, R. Correlating the Crystal Structure of A Thiol-Protected Au_{25} Cluster and Optical Properties. *J. Am. Chem. Soc.* **2008**, *130*, 5883.

(4) Ramakrishna, G.; Varnavskia, O.; Kimb, J.; Leeb, D.; Goodson, T.; Nonlinear Optical Properties of Quantum Sized Gold Clusters. In *Linear and nonlinear optics of organic materials VIII*, Proceedings of theSPIE The International Society for Optical Engineering,San Diego, CA,August 28, 2008; Jakubiak, R., Ed.; SPIE: Bellingham WA; Vol. 7049, p 70490L.1.

(5) Si, S.; Gautier, C.; Boudon, J.; Taras, R.; Gladiali, S.; Burgi, T. Ligand Exchange on Au_{25} Cluster with Chiral Thiols. *J. Phys. Chem. C* **2009**, *113*, 12966.

(6) Akola, J.; Walter, M.; Whetten, R. L.; Hakkinen, H.; Gronbeck, H. On the Structure of Thiolate-Protected Au_{25}. *J. Am. Chem. Soc.* **2008**, *130*, 3756.

(7) Heaven, M. W.; Dass, A.; White, P. S.; Holt, K. M.; Murray, R. W. Crystal Structure of the Gold Nanoparticle $[N(C_8H_{17})_4][Au_{25}(SCH_2CH_2Ph)_{18}]$. *J. Am. Chem. Soc.* **2008**, *130*, 3754.

(8) Walter, M.; Akola, J.; Lopez-Acevedo, O.; Jadzinsky, P. D.; Calero, G.; Ackerson, C. J.; Whetten, R. L.; Gronbeck, H.; Hakkinen, H. A unified view of ligand-protected gold clusters as superatom complexes. *Proc. Natl. Acad. Sci. U.S.A.* **2008**, *105*, 9157.

(9) Knight, W. D.; Clemenger, K.; deHeer, W. A.; Saunders, W. A.; Chou, M. Y.; Cohen, M. L. Electronic Shell Structure and Abundance of Sodium Clusters. *Phys. Rev. Lett.* **1984**, *52*, 2141.

(10) Ekardt, W. Dynamical Polarizability of Small Metal Particles: Self-Consistent Spherical Jellium Background Model. *Phys. Rev. Lett.* **1984**, *52*, 1925.

(11) Ekardt, W. Work function of small metal particles: Self-consistent spherical jellium-background model. *Phys. Rev. B: Condens. Matter Mater. Phys.* **1984**, *29*, 1558.

(12) Jiang, D.-E.; Dai, S. From Superatomic $Au25(SR)18-$ to Superatomic $M@Au24(SR)18q$ Core-Shell Clusters. *Inorg. Chem.* **2008**, *48*, 2720.

(13) Bishea, G. A.; Morse, M. D. Spectroscopic studies of jet-cooled AgAu and Au_2. *J. Chem. Phys.* **1991**, *95*, 5646.

Calculation of Absorption Spectra

J. Chem. Theory Comput., Vol. 6, No. 9, 2010 **2819**

(14) Klotzbucher, W. E.; Ozin, G. A. Optical Spectra of Hafnium, Tungsten, Rhenium, and Ruthenium Atoms and Other Heavy Transition-Metal Atoms and Small Clusters ($Zr_{1,2}$, $Pd_{1,2}$, $Au_{1,2,3}$) in Noble Gas Matrices. *Inorg. Chem.* **1980**, *19*, 3767.

(15) Simard, B.; Hackett, P. A. High Resolution Study of the (0, 0) and (1, 1) Bands of the AO_u^+-XO_g^+ System of Au_2. *J. Mol. Spectrosc.* **1990**, *142*, 310.

(16) Ames, L. L.; Barrow, R. F. Rotational analysis of bands of the gaseous Au_2 molecule. *Trans. Faraday Soc.* **1967**, *63*, 39.

(17) Morse, M. D. Clusters of Transition-Metal Atoms. *Chem. Rev.* **1986**, *86*, 1049.

(18) James, A. M.; Kowalcyk, P.; Simard, B.; Pinegar, J. C.; Morse, M. D. The $A'1_u$ <- X 0_g^+ System of Gold Dimer. *J. Mol. Spectrosc.* **1994**, *168*, 248.

(19) Harbich, W.; Fedrigo, S.; Buttet, J. Deposition of mass selected gold clusters in solid krypton. *J. Chem. Phys.* **1992**, *96*, 8104.

(20) Ermler, W. C.; Lee, Y. S.; Pitzer, K. S. Ab initio effective core potentials including relativistic effects. IV. Potential energy curves for the ground and several excited states of Au_2. *J. Chem. Phys.* **1979**, *70*, 293.

(21) Das, K. K.; Balasubramanian, K. Spectroscopic Properties of Low-Lying Electronic States of Au_2. *J. Mol. Spectrosc.* **1990**, *140*, 280.

(22) Itkin, I.; Zaitsevskii, A. Quasirelativistic multipartitioning perturbation theory calculations on electronic transitions in Au_2. *Chem. Phys. Lett.* **2003**, *374*, 143.

(23) Wang, X.; Wan, X.; Zhou, H.; Takami, S.; Kubo, M.; Miyamoto, A. Electronic structures and spectroscopic properties of dimers Cu_2, Ag_2, and Au_2 calculated by density functional theory. *J. Mol. Struct. (Theochem)* **2002**, *579*, 221.

(24) Jiang, D.-e.; Whetten, R. L.; Luo, W.; Dai, S. The smallest thiolated gold superatom complexes. *J. Phys. Chem. C* **2009**, *113*, 17291.

(25) Gronbeck, H.; Walter, M.; Hakkinen, H. Theoretical Characterization of Cyclic Thiolated Gold Clusters. *J. Am. Chem. Soc.* **2006**, *128*, 10268.

(26) Aikens, C. M. Effects of Core Distances, Solvent, Ligand, and Level of Theory on the TDDFT Optical Absorption Spectrum of the Thiolate-Protected Au25 Nanoparticle. *J. Phys. Chem. A* **2009**, *113*, 10811.

(27) Negishi, Y.; Nobusada, K.; Tsukuda, T. Glutathione-Protected Gold Clusters Revisited: Bridging the Gap between Gold(I)-Thiolate Complexes and Thiolate-Protected Gold Nanocrystals. *J. Am. Chem. Soc.* **2005**, *127*, 5261.

(28) Negishi, Y.; Chaki, N. K.; Shichibu, Y.; Whetten, R. L.; Tsukuda, T. Origin of Magic Stability of Thiolated Gold Clusters: A Case Study on $Au_{25}(SC_6H_{13})_{18}$. *J. Am. Chem. Soc.* **2007**, *129*, 11322.

(29) Stener, M.; Nardelli, A.; Francesco, R. D.; Fronzoni, G. Optical Excitations of Gold Nanoparticles: A Quantum Chemical Scalar Relativistic Time Dependent Density Functional Study. *J. Phys. Chem. C* **2007**, *111*, 11862.

(30) Rumi, M.; Ehrlich, J. E.; Heikal, A. A.; Perry, J. W.; Barlow, S.; Hu, Z.; McCord-Maughon, D.; Parker, T. C.; Rockel, H.; Thayumanavan, S.; Marder, S. R.; Beljonne, D.; Bredas, J.-L. Structure-property relationships for two-photon absorbing chromophores: bis-donor diphenylpolyene and bis(styryl)benzene derivatives. *J. Am. Chem. Soc.* **2000**, *122*, 9500.

(31) Sutherland, R. L.; Nonlinear Absorption In *Handbook of Nonlinear Optics*; Thompson, B. J., Ed.; Marcel Dekker, Inc.: New York, 1996.

(32) Day, P. N.; Nguyen, K. A.; Pachter, R. TDDFT Study of One- and Two-Photon Absorption Properties: Donor-pi-Acceptor Chromophores. *J. Phys. Chem. B* **2005**, *109*, 1803.

(33) Day, P. N.; Nguyen, K. A.; Pachter, R. Calculation of two-photon absorption spectra of donor-acceptor compounds in solution using quadratic response time-dependent density functional theory. *J. Chem. Phys.* **2006**, *125*, 094103.

(34) Day, P. N.; Nguyen, K. A.; Pachter, R. Calculation of One-Photon and Two-Photon Absorption Spectra of Porphyrins Using Time-Dependent Density Functional Theory. *J. Chem. Theory Comput.* **2008**, *4*, 1094–1106.

(35) Orr, B. J.; Ward, J. F. perturbation theory of the non-linear optical polarization of an isolated system. *Mol. Phys.* **1971**, *20*, 513.

(36) Birge, R. R.; Pierce, B. M. A theoretical analysis of the two-photon properties of linear polyenes and the visual chromophores. *J. Chem. Phys.* **1979**, *70*, 165.

(37) Birge, R. R.; Bennett, J. A.; Hubbard, L. M.; Fang, H. L.; Pierce, B. M.; Kliger, D. S.; Leroi, G. E. Two-Photon Spectroscopy of all-trans-Retinal. Nature of the Low-Lying Singlet States. *J. Am. Chem. Soc.* **1982**, *104*, 2519.

(38) Peticolas, W. L. Multiphoton spectroscopy. *Annu. Rev. Phys. Chem.* **1967**, *18*, 233.

(39) McClain, W. M. Two-Photon Molecular Spectroscopy. *Acc. Chem. Res.* **1974**, *7*, 129.

(40) Monson, P. R.; McClain, W. M. Polarization dependence of the two-photon absorption of tumbling molecules with application to liquid 1-chloronaphthalene and benzene. *J. Chem. Phys.* **1970**, *53*, 29.

(41) Gold, A. *Proceedings of the International School of Physics*; Academic: New York, 1969.

(42) McClain, W. M. Excited State Symmetry Assignment Through Polarized Two-Photon Absorption Studies of Fluids. *J. Chem. Phys.* **1971**, *55*, 2789.

(43) Masthay, M. B.; Findsen, L. A.; Pierce, B. M.; Bocian, D. F.; Lindsey, J. S.; Birge, R. R. a theoretical investigation of the one- and two-photon properties of porphyrins. *J. Chem. Phys.* **1986**, *84*, 3901.

(44) Albota, M.; Beljonne, D.; Bredas, J. L.; Ehrlich, J. E.; Fu, J. Y.; Heikal, A. A.; Hess, S. E.; Kogej, T.; Levin, M. D.; Marder, S. R.; McCord-Maughon, D.; Perry, J. W.; Rockel, H.; Rumi, M.; Subramaniam, G.; Webb, W. W.; Wu, X. L.; Xu, C. design of organic molecules with large two-photon absorption cross-sections. *Science* **1998**, *281*, 1653.

(45) Karotki, A.; Drobizhev, M.; Dzenis, Y.; Taylor, P. N.; Anderson, H. L.; Rebane, A. Dramatic enhancement of intrinsic two-photon absorption in a conjugated porphyrin dimer. *Phys. Chem. Chem. Phys.* **2004**, *6*, 7.

(46) Spangler, C. W.; Starkey, J. R.; Meng, F.; Gong, A.; Drobizhev, M.; Rebane, A.; Moss, B.; Targeted Two-photon Photodynamic Therapy for the Treatment of Subcutaneous Tumors. In *Optical Methods for Tumor Treatment and Detection: Mechanisms and Techniques in Photodynamic Therapy XIV*; Proceedings of theSPIE-The International Society for Optical Engineering, Bellingham, WA, April 5, 2005; Kessel, D.,Ed.; SPIE: Bellingham, WA; Vol. 5689, p 141.

2820 *J. Chem. Theory Comput., Vol. 6, No. 9, 2010*

Day et al.

(47) Kirkpatrick, S. M.; Baur, J. W.; Clark, C. M.; Denny, L. R.; Tomlin, D. W.; Reinhardt, B. R.; Kannan, R.; Stone, M. O. Holographic recording using two-photon-induced photopolymerization. *Appl. Phys. A: Mater. Sci. Process.* **1999**, *69*, 461.

(48) Nguyen, K. A.; Day, P. N.; Pachter, R. Effects of solvation on one- and two-photon spectra of coumarin derivatives: A time-dependent density functional theory study. *J. Chem. Phys.* **2007**, *126*, 094303.

(49) Wang, J.; Blau, W. J. Inorganic and hybrid nanostructures for optical limiting. *J. Opt. A: Pure Appl. Opt.* **2009**, *11*, 024001.

(50) Castro, A.; Marques, M. A. L.; Romero, A. H.; Oliveira, M. J. T.; Rubio, A. The role of dimensionality on the quenching of spin-orbit effects in the optics of gold nanostructures. *J. Chem. Phys.* **2008**, *129*, 144110.

(51) Douglas, M.; Kroll, N. M. Quantum Electrodynamical Corrections to the Fine Structure of Helium. *Ann. Phys.* **1974**, *82*, 89.

(52) Hess, B. A. Relativistic electronic-structure calculations employing a two-component no-pair formalism with external-field projection operators. *Phys. Rev. A: At., Mol., Opt. Phys.* **1986**, *33*, 3742.

(53) Schmidt, M. W.; Baldridge, K. K.; Boatz, J. A.; Elbert, S. T.; Gordon, M. S.; Jensen, J. H.; Koseki, S.; Matsunaga, N.; Nguyen, K. A.; Su, S.; Windus, T. L.; Dupuis, M.; Montgomery, J. General Atomic and Molecular Electronic Structure System. *J. Comput. Chem.* **1993**, *14*, 1347.

(54) Agren, H., personal communication.

(55) *Dalton, a molecular electronic structure program*, release 2.0; KTH: Stockholm, Sweden, 2005; http://www.kjemi.uio.no/software/dalton/dalton.html. Accessed March 4, 2005.

(56) van Lenthe, E.; Baerends, E. J.; Snijders, J. G. Relativistic regular two-component Hamiltonians. *J. Chem. Phys.* **1993**, *99*, 4597.

(57) van Lenthe, E.; Baerends, E. J.; Snijders, J. G. Relativistic total energy using regular approximations. *J. Chem. Phys.* **1994**, *101*, 9783.

(58) *ADF*, release 2008.01; SCM, Theoretical Chemistry, Vrije Universiteit: Amsterdam, The Netherlands, 2008; http://www.scm.com. Accessed November 12, 2008.

(59) teVelde, G.; Bickelhaupt, F. M.; Gisbergen, S. J. A. v.; Guerra, C. F.; Baerends, E. J.; Snijders, J. G.; Ziegler, T. Chemistry with ADF. *J. Comput. Chem.* **2001**, *22*, 931.

(60) Guerra, C. F.; Snijders, J. G.; Velde, G. t.; Baerends, E. J. Towards an order-N DFT method. *Theor. Chem. Acc.* **1998**, *99*, 391.

(61) Wang, F.; Ziegler, T. A simplified relativistic time-dependent density-functional theory formalism for the calculations of excitation energies including spin-orbit coupling effect. *J. Chem. Phys.* **2005**, *123*, 154102.

(62) Wang, F.; Ziegler, T.; van Lenthe, E.; van Gisbergen, S.; Baerends, E. J. The calculation of excitation energies based on the relativistic two-component zeroth-order regular approximation and time-dependent density-functional with full use of symmetry. *J. Chem. Phys.* **2005**, *122*, 204103.

(63) Becke, A. D. Density-functional exchange-energy approximation with correct asymptotic behavior. *Phys. Rev. A: At., Mol., Opt. Phys.* **1988**, *38*, 3098.

(64) Perdew, J. P. Density-functional approximation for the correlation energy of the inhomogeneous electron gas. *Phys. Rev. B: Condens. Matter Mater. Phys.* **1986**, *33*, 8822.

(65) Lovallo, C. C.; Klobukowski, M. Improved Model Core Potentials for the Second- and Third-Row Transition Metals. *J. Comput. Chem.* **2004**, *25*, 1206–1213.

(66) Slater, J. C. A simplification of the Hartree-Fock Method. *Phys. Rev.* **1951**, *81*, 385.

(67) Tsuchiya, T.; Abe, M.; Nakajima, T.; Hirao, K. Accurate relativistic Gaussian basis sets for H through Lr determined by aomic SCF calculations with the third-order Douglas-Kroll approximation. *J. Chem. Phys.* **2001**, *115*, 4463.

(68) Tsuchiya, T.; Abe, M.; Nakajima, T.; Hirao, K. Accurate relativistic Gaussian basis sets for H through Lr determined by atomic SCF calculations with the third-order Douglas-Kroll approximation; Riken: Wako, Saitama; http://www.riken.jp/qcl/publications/dk3bs/periodic_table.html. Accessed May 4, 2010.

(69) Hay, P. J.; Wadt, W. R. Ab initio effective core potentials for molecular calculations. Potentials for K to Au including the outermost core orbitals. *J. Chem. Phys.* **1985**, *82*, 299.

(70) Andrae, D.; Haeussermann, U.; Dolg, M.; Stoll, H.; Preus, H. Energy-adjusted ab initio pseudopotentials for the second and third row transition elements. *Theor. Chim. Acta* **1990**, *77*, 123.

(71) Bergner, A.; Dolg, M.; Küchle, W.; Stoll, H.; Preuss, H. Ab-initio energy-adjusted pseudopotentials for elements of groups 13−17. *Mol. Phys.* **1993**, *80*, 1431.

(72) Becke, A. D. B3LYP: Density-functional thermochemistry III. *J. Chem. Phys.* **1993**, *98*, 5648.

(73) Lee, C.; Yang, W.; Parr, R. G. Development of the Colle-Salvetti correlation-energy formula into a functional of the electron-density. *Phys. Rev. B: Condens. Matter Mater. Phys.* **1988**, *37*, 785.

(74) Vosko, S. H.; Wilk, L.; Nusair, M. Accurate spin-dependent electron liquid correlation energies for local spin density calculations: a critical analysis. *Can. J. Phys. Chem.* **1980**, *58*, 1200.

(75) Stephens, P. J.; Devlin, F. J.; Chabalowski, C. F.; Frisch, M. J. Ab initio Calculation of Vibrational absorption and circular dichroism spectra using density functional force fields. *J. Phys. Chem.* **1994**, *98*, 11623.

(76) Yanai, T.; Tew, D. P.; Handy, N. C. A new hybrid exchange-correlation functional using the Coulomb-attenuating method (CAM-B3LYP). *Chem. Phys. Lett.* **2004**, *393*, 51.

(77) Schipper, P. R. T.; Gritsenko, O. V.; van Gisbergen, S. J. A.; Baerends, E. J. Molecular calculations of excitation energies and (hyper)polarizabilities with a statistical average of orbital model exchange-correlation potentials. *J. Chem. Phys.* **2000**, *112*, 1344.

(78) Piecuch, P.; Kucharski, S. A.; Kowalski, K.; Musial, M. Efficient computer implementation of the renormalized coupled-cluster methods: The R-CCSD[T], R-CCSD(T), CR-CCSD[T], and CR-CCSD(T) approaches. *Comput. Phys. Commun.* **2002**, *149*, 71.

(79) Kowalski, K.; Piecuch, P. New coupled-cluster methods with singles, doubles, and noniterative triples for high accuracy calculations of excited electronic states. *J. Chem. Phys.* **2004**, *120*, 1715.

Calculation of Absorption Spectra

J. Chem. Theory Comput., Vol. 6, No. 9, 2010 **2821**

(80) Wloch, M.; Gour, J. R.; Kowalski, K.; Piecuch, P. Extension of renormalized coupled-cluster methods including triple excitations to excited electronic states of open-shell molecules. *J. Chem. Phys.* **2005**, *122*, 214107.

(81) Christiansen, O.; Koch, H.; Halkier, A.; Jorgensen, P.; Helgaker, T.; Meras, A. S. d. Large-scale calculations of excitation energies in coupled cluster theory: The singlet excited states of benzene. *J. Chem. Phys.* **1996**, *105*, 6921.

(82) Olsen, J.; Jorgensen, P. Linear and nonlinear response functions for an exact state and for an MCSCF state. *J. Chem. Phys.* **1985**, *82*, 3235.

(83) Hettema, H.; Jensen, H. J. A.; Jorgensen, P.; Olsen, J. Quadratic response functions for a multiconfigurational self-consistent field wave function. *J. Chem. Phys.* **1992**, *97*, 1174.

(84) Furche, F. On the density matrix based approach to time-dependent density functional response theory. *J. Chem. Phys.* **2001**, *114*, 5982.

(85) Salek, P.; Vahtras, O.; Guo, J.; Luo, Y.; Helgaker, T.; Agren, H. Calculations of two-photon absorption cross-sections by means of density-functional theory. *Chem. Phys. Lett.* **2003**, *374*, 446.

(86) Agren, H.; Norman, P.; Baev, A. Multiphysics Modelling of Optical Materials. In *Optical Materials in Defence Systems Technology III*; Grote, J. G., Kajzar, F., Lindgren, M., Eds.; SPIE: Stockholm, Sweden, 2006; Vol. 6401, p 640103.

(87) Zhao, Y.; Truhlar, D. G. The M06 suite of density functionals for main group thermochemistry, thermochemical kinetics, noncovalent interactions, excited states, and transition elements: two new functionals and systematic testing of four M06-class functionals and 12 other functionals. *Theor. Chem. Acc.* **2008**, *120*, 215.

(88) Grimme, S. Semiempirical GGA-Type Density Functional Constructed with a Long-Range Dispersion Correction. *J. Comput. Chem.* **2006**, *27*, 1787.

(89) Aikens, C. M. Origin of Discrete Optical Absorption Spectra of M25(SH)18 - Nanoparticles (M = Au, Ag). *J. Phys. Chem. C* **2008**, *112*, 19797–19800.

(90) Jiang, D.-e.; Chen, W.; Whetten, R. L.; Chen, Z. What Protects the Core When the Thiolated Au Cluster is Extremely Small. *J. Phys. Chem. C* **2009**, *113*, 16983–16987.

(91) Tao, J. M.; Perdew, J. P.; Staroverov, V. N.; Scuseria, G. E. Climbing the Density Functional Ladder: Nonempirical Meta-Generalized Gradient Approximation Designed for Molecules and Solids. *Phys. Rev. Lett.* **2003**, *91*, 146401.

(92) Perdew, J. P.; Burke, K.; Ernzerhof, M. Generalized Gradient Approximation Made Simple. *Phys. Rev. Lett.* **1996**, *77*, 3865.

(93) Zhang, Y.; Shuang, S.; Dong, C.; Lo, C. K.; Paau, M. C.; Choi, M. M. F. Application of HPLC and MALDI-TOF MS for Studying As-Synthesized Ligand-Protected Gold Nano-clusters Products. *Anal. Chem.* **2009**, *81*, 1676.

(94) Aikens, C. M. Origin of Discrete Optical Absorption Spectra of M25(SH)18 - Nanoparticles (M = Au, Ag). *J. Phys. Chem. C* **2008**, *112*, 19797–19800.